

# A356/TiO<sub>2</sub> Nanocomposite Fabricated by Friction Stir Processing: Microstructure, Mechanical Properties and Tribologic Behavior

S. AHMADIFARD,<sup>1</sup> SH. KAZEMI,<sup>1,3,4</sup> and A. MOMENI<sup>2</sup>

1.—Faculty of Engineering, Bu-Ali Sina University, Hamedan, Iran. 2.—Materials Science and Engineering Department, Hamedan University of Technology, Hamedan, Iran. 3.—e-mail: shahab.kazemi@basu.ac.ir. 4.—e-mail: shkazemiir@yahoo.com

In this research, the effects of friction stir processing (FSP) and nano TiO<sub>2</sub> particles on the microstructure, mechanical and tribologic properties of A356 Al alloy were investigated. The starting dendritic structure transformed into the Al matrix with a uniform distribution of Si-rich particles due to FSP. The results showed that FSP improves the nano-hardness and elastic modulus by 11% and 6%, respectively. The combined effects of FSP and nano TiO<sub>2</sub> could raise the hardness and elastic modulus of the composite by 87% and 16% with respect to those of the base metal. The law of mixture rule was modified to relate the hardness and elastic modulus of the composite to those of the constituents. The results of wear tests showed that the mechanism of wear changes from adhesive in the base metal to abrasive in the fabricated composite.

## INTRODUCTION

The mechanical properties and processing of aluminum alloys have been the topic of numerous studies for decades.<sup>1,2</sup> Despite some attractive properties, low strength and weak wear resistance are the major drawbacks of Al alloys. Making composites with different ceramic materials has been found to be a simple way of improving the strength of metallic matrices. The mechanical properties of aluminum matrix composites (AMCs) mainly depend on the nature of the reinforcing material and the manufacturing technique. Based on this concept, various types of reinforcing particles such as SiC,<sup>3,4</sup> Al<sub>2</sub>O<sub>3</sub>,<sup>5,6</sup> Si<sub>3</sub>N<sub>4</sub>,<sup>7</sup> B<sub>4</sub>C,<sup>8–10</sup> ZrO<sub>2</sub><sup>11</sup> and TiO<sub>2</sub><sup>12</sup> have been assigned in AMCs. The fabricated AMCs have been successfully used in various industries. For example, AMCs with the incorporation of Al<sub>2</sub>O<sub>3</sub> or SiC particles in A356 have been used as pistons, cylinder heads and connecting rods in the automotive industry.<sup>13–15</sup>

Friction stir processing (FSP) is a solid-state surface processing in which a tool with its rotational and traverse movement applies severe plastic deformation on the surface layers.<sup>16–18</sup> It can be used for the modification of microstructure and the

fabrication of surface composites. In cast alloys, FSP removes the cast defects and improves mechanical properties and wear resistance.<sup>19–21</sup> FSP has been used to modify the microstructure and mechanical properties of Al-Si alloys.<sup>22–24</sup> Alidokht et al.<sup>25</sup> showed that FSP improves the wear behavior of A356 because of the significant microstructural modifications. Yang et al.<sup>26</sup> studied the properties of Al<sub>3</sub>Ti/A356 composites fabricated by in situ casting after multi-pass FSP. The improved strength and ductility were ascribed to grain refinement, porosity removal and the uniform dispersion of Al<sub>3</sub>Ti and Si particles in the matrix. Shojaeefard et al.<sup>27</sup> investigated the effect of various reinforcing particles in A356 matrix and found that the specific strength of the reinforcing particle and quality of the interface with the matrix are the major parameters involved in the strength of AMCs. Two other investigations in A356 and LM25 showed that FSP modifies the microstructure and improves the mechanical properties.<sup>28,29</sup> However, Baruch et al.<sup>30</sup> claimed that multi-pass FSP degrades the hardness of AS7U3G cast alloy because of the decrease in the dislocation density. Even though the capability of FSP in fabricating various metal matrix composites has been well documented, the

microstructure and mechanical properties of AMCs fabricated by using different types of reinforcing particles are still being investigated. Hence, current research has aimed to study the microstructure and mechanical properties of A356-TiO<sub>2</sub> nanocomposite fabricated by FSP.

## EXPERIMENTAL PROCEDURE

The starting material in this research was A356 Al alloy received in the as-cast condition. The nano-sized TiO<sub>2</sub> particles with average particle size of 40–60 nm (supplier: TECNON, S.L. Co.) were used as the reinforcing material.

The tool was machined from H13 tool steel with a shoulder of 20 mm diameter and a threaded pin (M7 × 1.0) of 4 mm length and 7 mm diameter [see Supplementary Fig. S1(a)]. After machining, the tool hardened to reach the hardness of 55 HRC. A groove (1 mm wide and 3 mm deep) was machined in the middle of the workpiece and filled with the reinforcing particles. A “pinless” FSP tool [see Supplementary Fig. S1(b)], was initially used to cover the groove and prevent the particles from dissipating and escaping from the FSP zone. A FSP machine (11 kW, 40 kN) was used to fabricate the surface composite as shown schematically in Supplementary Fig. S1(c).

The specimens were clamped in a fixture and processed with the traverse speed of 80 mm min<sup>-1</sup>, rotation speed of 1100 rpm and tilt of 2° in the spindle toward trailing direction.

After FSP, the samples were sectioned in planes perpendicular to the processing direction and prepared for the metallographic analyses. After etching with Keller's reagent (1 ml 48% HF, 1.5 ml HCl and 10 ml nitric acid in 87.5 ml distilled water for 30 s) the transverse sections were examined by optical and field emission scanning electron (FESEM: JEOL JSM-840A) microscopes.

The hardness profile was determined using a Vickers indenter at the load of 100 g and dwell time of 10 s. The average of three measurements was calculated and reported as the microhardness value.

The hardness and elastic modulus of the as-received material and FSPed samples were determined using the load-penetration depth curves obtained from the nanoindentation tests (NHTX S/N: 01-03119, CSM Instruments with a Berkovich diamond indenter, B-J87). The indentations were carried out at loading and unloading rates of 140 mN/min up to a maximum load of about 30 mN. To take the repeatability into account, the test results were acquired from the average of four indents. The hardness and elastic modulus were calculated by the standard procedure.<sup>31</sup>

Friction and wear properties of the samples were investigated using a reciprocating test machine in which AISI 52100 steel with the hardness of 63 HRC was used as the pin (5 mm diameter). The wear sample was 4 × 1 cm and wear test was

performed in the SZ of FSPed samples. The tests were conducted at room temperature and 30–40% humidity with a sliding speed of 0.2 m s<sup>-1</sup> under an applied load of 10 N. The sliding distance was 500 m and the tests were carried out in the unlubricated condition. The mass loss of the specimens was measured at 50-m intervals in the sliding distance, using analytical scales with 0.1-mg precision. The friction coefficient between the surface and pin was continuously recorded during the wear tests. To take the repeatability into account, the wear test results were acquired from the average of four readings. The surface roughness (Ra) was also measured after wear tests using a profilometer model Mitutoyo to calculate the total depths of wear tracks and total wear rates. Finally, the worn surfaces were studied by SEM.

## RESULTS AND DISCUSSION

### Microstructural Observations

Figure 1 shows the optical and SEM micrographs of the as-received material before and after FSP. Figure 1a shows that the microstructure of A356 before FSP is characterized by a dendritic structure. The dendrite core is mainly rich in Al and solidifies as the first solid phase. When the dendrites form, Si is expelled into the liquid, which finally solidifies into an Si-rich phase by the eutectic transformation.<sup>32</sup> Supplementary Fig. S2 shows the SEM images and EDS analyses from the core of the dendrites and the interdendritic phase observed in Fig. 1a. The EDS analyses confirm that the core of the dendrite is rich in Al, while the interdendritic phase is almost rich in Si.

Figure 1b shows that the regions of the “stir zone” (SZ) and “thermomechanically affected zone” (TMAZ) in the FSPed sample are characterized by different microstructural features. In the SZ region the dendritic structure has been completely replaced with a uniform fine microstructure. It appears that the large strain accompanied by high temperature has led to the transformation of the cast structure into an ultrafine grain structure. The heavy plastic deformation and subsequent dynamic recrystallization should be the underlying phenomena for the observed structural changes.<sup>33</sup>

The magnified image of SZ in Fig. 1c shows that the dendritic structure has been completely dissolved into an integrated matrix of  $\alpha$ -Al containing refined and uniformly distributed Si-rich particles. The micrograph of Fig. 1b shows that the microstructure of TMAZ is still dendritic. However, a change in the morphology of dendrites from the tree-type into globular has taken place. In TMAZ, high temperature and medium strains provide the favorable condition for breaking down the secondary branches of dendrites and their gradual globularization. The dissociation of long dendrites and secondary arms has been found as the primary step

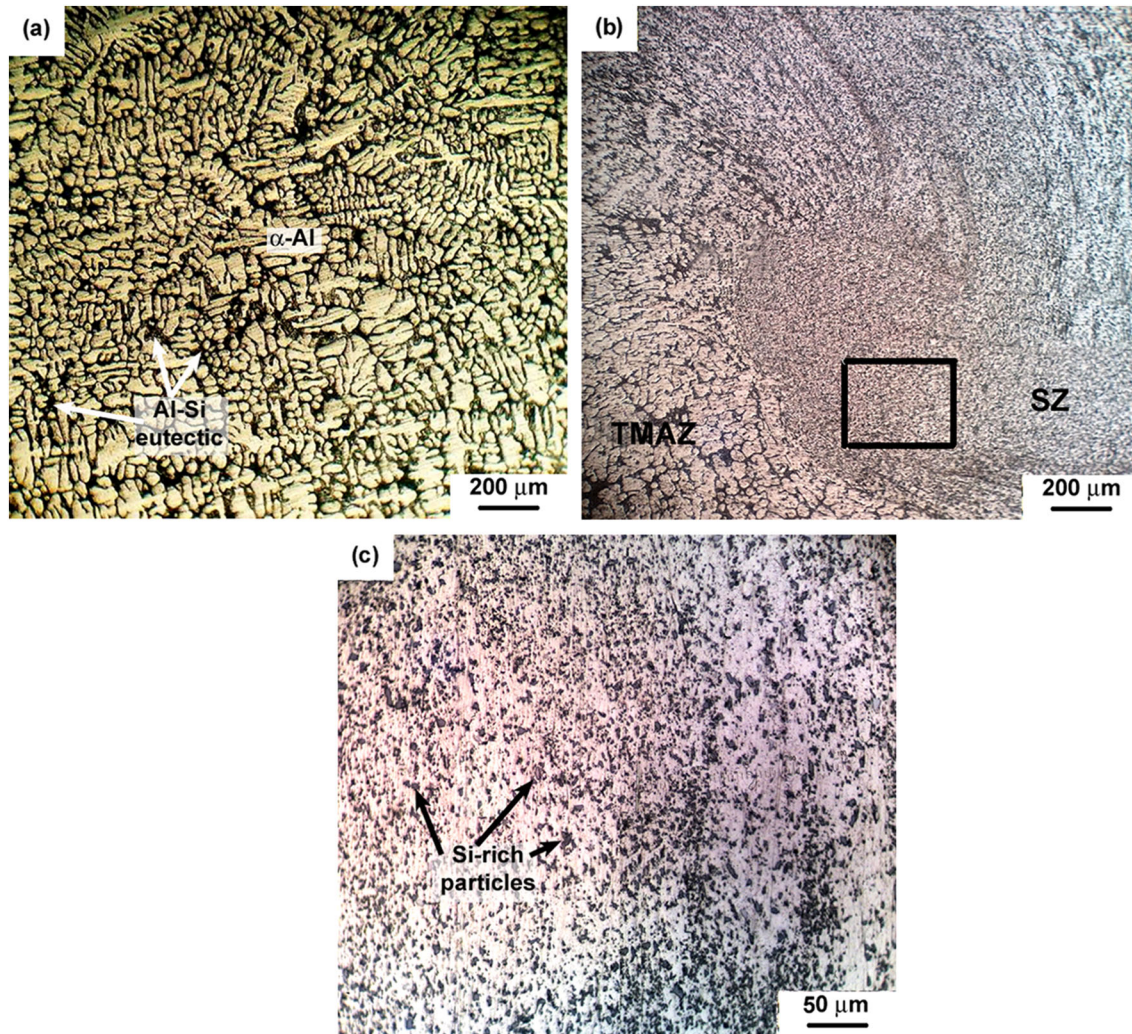


Fig. 1. Optical micrographs from (a) the starting material comprised of the dendritic structure of alpha Al and Al-Si eutectic as the interdendritic phase, (b) microstructure of the stir zone (SZ) and thermomechanical affected zone (TMAZ) in the FSPed sample and (c) the magnified view of the area selected in (b) showing the Si-rich particles dispersed within the Al matrix in SZ.

in the transformation of a cast structure into a wrought one.

Figure 2 shows the FESEM images from the fabricated AMC (Fig. 2a and b) and the EDS analysis (Fig. 2c) from the nanoparticle highlighted in Fig. 2b. The micrograph of Fig. 2a indicates that a nearly uniform distribution of  $\text{TiO}_2$  nanoparticles has been obtained after one pass of FSP. The magnified image in Fig. 2b and the corresponding EDS spectrum in Fig. 2c clearly show that the cubic  $\text{TiO}_2$  nanoparticles have been well distributed within the matrix and particle agglomeration is hardly visible. It is generally expected that nanoparticles agglomerate and make larger particles to reduce their surface energy when exposed to high temperatures. This phenomenon easily occurs when AMCs are produced by melting processes such as compositing.<sup>32</sup> However, the solid state processing in FSP facilitates the uniform distribution of reinforcing particles without considerable particle agglomeration.

In addition to the type of reinforcing particles, their distribution within the matrix has a crucial effect on the mechanical properties of composites. A uniform distribution of particles gives rise to the homogeneous mechanical properties, especially higher ductility. In contrast, the heterogeneously dispersed particles lead to the localized deformation and commonly premature fracture.

### Mechanical Properties

The microhardness profiles of the FSPed samples (FSPed base metal and AMC) and base metal (BM) are compared in Fig. 3. The results of Fig. 3a show that the hardness increases from about 48 HV for the unprocessed BM to 54 HV for the FSPed BM ( $\sim 13\%$  improvement).

The highest hardness is obtained in the center part of the SZ (in  $\pm 3.5$  mm from the centerline of FSP) where strain and temperature are maximized. In the marginal zone of SZ, i.e., 5–7 mm out of the

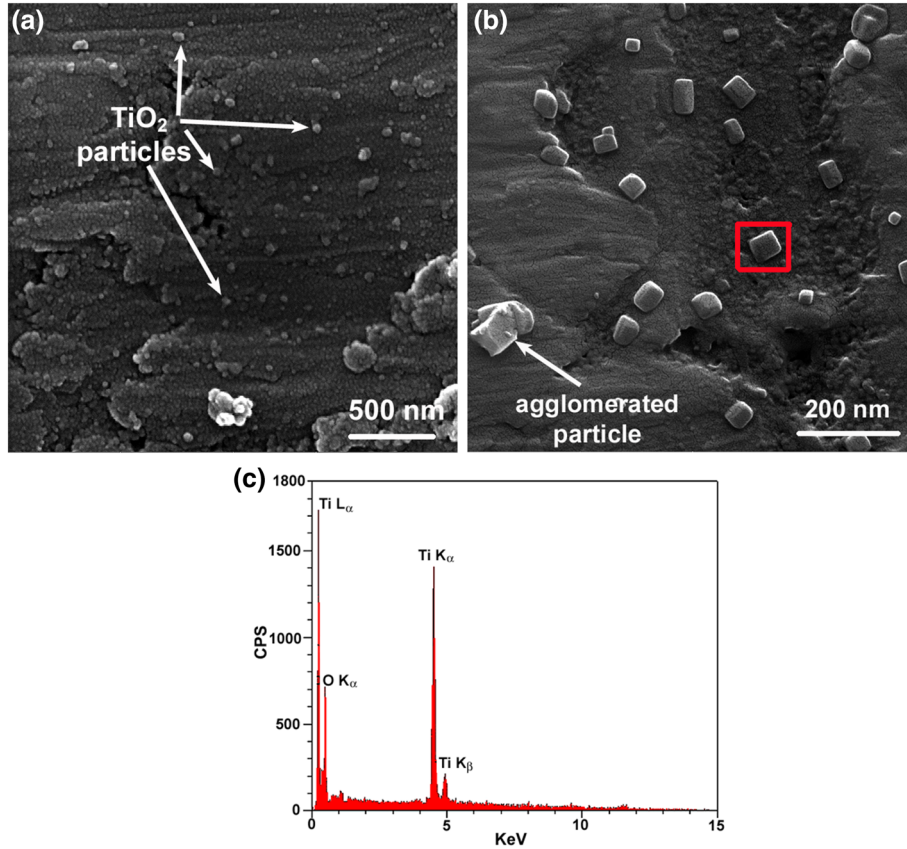


Fig. 2. (a, b) FESEM images with two different magnifications from the SZ of fabricated aluminum matrix composite (AMC) showing the uniform distribution of TiO<sub>2</sub> nanoparticles within the matrix and (c) EDS analysis of particle highlighted in (b).

centerline, the hardness abruptly decreases and reaches that of the unprocessed BM. It is clear that the decrease in hardness occurs in the TMAZ and heat-affected zone (HAZ). In the TMAZ, lower temperature and strain than those in the SZ reduce the rate of microstructural modification and lead to lower strength.<sup>34</sup> In the HAZ, the heating cycle takes place without strain, leading to the grain enlargement and lower hardness. Figure 3b clearly shows the locations of the SZ, TMAZ and HAZ on the detailed hardness curve for half of the FSP zone. Referring to the microstructures shown in Figs. 1 and 2, the improved hardness in the SZ of FSPed BM can be attributed to the considerable microstructural modification appearing as the dissociation of the dendritic structure and the uniform distribution of fine Si-rich particles in the matrix. As shown in Fig. 3a, the hardness of the one-pass processed AMC increased about 52% (from 48 to 73 HV) because of the superimposed effects of microstructural modification and distribution of hard TiO<sub>2</sub> nanoparticles.

Figure 4 exhibits the results of nanoindentation (NI) tests on the studied samples.

It is observed that the samples have been loaded to a maximum value of 30 mN before unloading. The depth of penetration ( $h_c$ ) and contact area ( $A_c$ )

are the quantities that are often measured in NI tests. The nano-hardness ( $H$ ) can be simply determined by dividing the maximum load ( $P_{max}$ ) by the contact area as follows:

$$H = \frac{P_{max}}{A_c} \quad (1)$$

This method can be also used to measure the elastic moduli of surface composites. Young's modulus ( $E$ ) can be calculated using the reduced Young's modulus ( $E_r$ ), which is determined from the slope of the unloading curves of Fig. 4, as follows:<sup>31</sup>

$$E_r = \frac{\sqrt{\pi}}{2\sqrt{A_c}} \cdot \left. \frac{dP}{dh} \right|_{P_{Max}} \quad (2)$$

Assuming the elastic constants of the indenter as  $\nu_i = 0.07$  and  $E_i = 1140$  GPa, Young's modulus can be calculated using the following equation:<sup>35</sup>

$$E = (1 - \nu^2) / \left\{ \left( \frac{1}{E_r} \right) - \left( \frac{1 - \nu_i^2}{E_i} \right) \right\} \quad (3)$$

The results of NI tests are summarized in Table I.

The values of  $E$  and  $G$  calculated for the BM agree well with those reported in the literature.<sup>36</sup> It is inferred that porosities or other defects in the

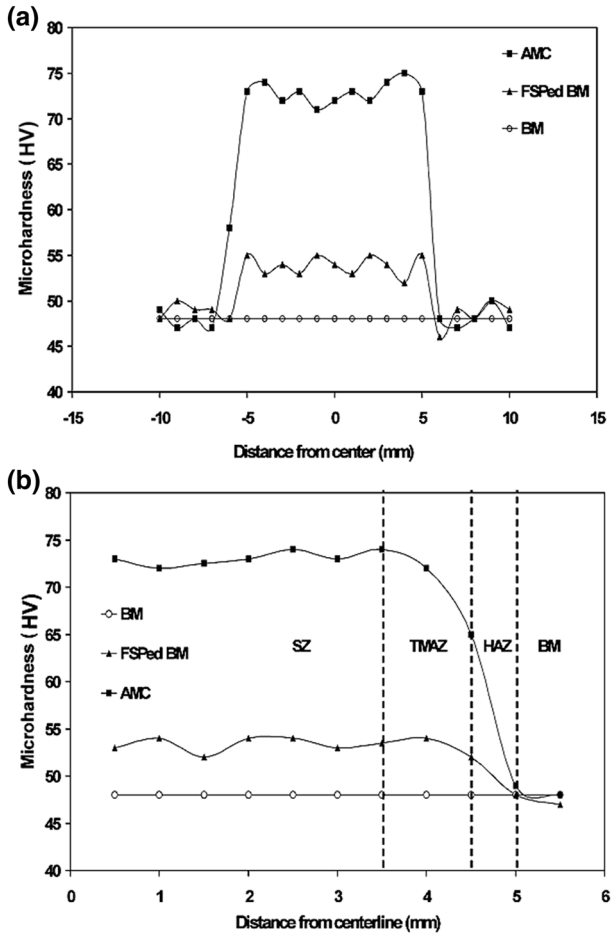


Fig. 3. Microhardness results for different samples: (a) profile of microhardness in the width of samples and (b) profile of microhardness for the half width of the sample showing the locations of the SZ, TMAZ, HAZ and BM regions.

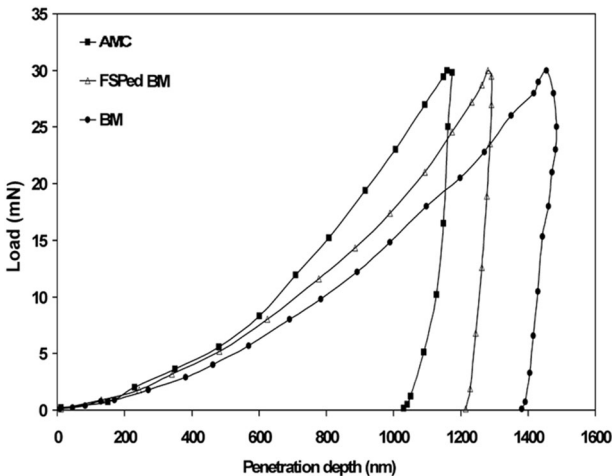


Fig. 4. Load-displacement results obtained from the nanoindentation test applied to the samples.

sample cannot affect the results of NI tests, and the calculated values of  $E$  and  $G$  are actually the real values of the composites.

The results in Table I show that the nano-hardness and elastic modulus of BM after FSP are improved by 10% and 6%, respectively. Further, for the fabricated AMC, the nano-hardness and elastic modulus increase about 69% and 9% higher than those for the FSPed BM. It appears that the incorporation of  $\text{TiO}_2$  increases the effectiveness of FSP in raising the mechanical properties of the A356 matrix.

The load–displacement relationship for various indenter types has been proposed as a power-law equation, given by:<sup>31</sup>

$$P = \beta h^m \quad (4)$$

where  $\beta$  and  $m$  are constants. Based on Eq. 4, the plots of P–h can be drawn in log–log window, as shown in Fig. 5.

It is observed that the values of  $m$  for BM and FSPed BM are nearly identical as 1.58 and the value of  $\ln \beta$  is about 8. However, for the fabricated AMC, the values of  $m$  and  $\ln \beta$  have increased to 1.72 and 8.8, respectively. According to the literature,  $m$  only depends on the indenter geometry and takes a constant value of 1 for flat cylinders, 2 for cones and 1.5 for spheres.<sup>31</sup> The increase in the value of  $m$  for AMC illustrates the further work-hardening rate due to the  $\text{TiO}_2$  nanoparticles. The geometrical analysis shows that for a Berkovich indenter, Eq. 4 can be elaborately formulated as follows:<sup>37</sup>

$$P = \left\{ \left( 3\sqrt{3}H \tan^2 \theta \right)^{-1/2} + \left[ \frac{2(\pi - 2)}{\pi} \right] \left( \frac{\sqrt{\pi H}}{2E} \right) \right\}^{-1} h^2 \quad (5)$$

here  $\theta$  is the face angle of the Berkovich indenter ( $65.27^\circ$ ), and  $H$  and  $E$  are the hardness and elastic modulus, respectively. According to Eq. 5, the value of  $m$  is 2 and independent of the material specification. However, the current results show that both  $m$  and  $\beta$  depend on the materials characteristics so that they slightly decrease as the hardness of the workpiece increases. It is evident that the addition of nano  $\text{TiO}_2$  particles has changed the P–h variation. This can be attributed to change in the mechanism of work hardening from dislocation interaction to the interaction of dislocations with nano  $\text{TiO}_2$  particles. The role of nano  $\text{TiO}_2$  particles in the hardness and work-hardening behavior of fabricated AMC can be studied by the Hall–Petch equation.

To establish a relationship between the mechanical properties of a composite, such as the hardness or elastic modulus, with the same properties of its constituents has been a great challenge for researchers. The law of mixture rule and shear lag are two of the most famous models. However, it has been shown that the general form of these models is simpler than being able to accurately consider the actual interaction between constituents of a

**Table I. Nanoindentation results of the studied samples**

| Parameter                            | Sample            |                    |                    | Dimension       |
|--------------------------------------|-------------------|--------------------|--------------------|-----------------|
|                                      | BM                | FSPed BM           | AMC                |                 |
| Contact area ( $A_c$ )               | $4.2 \times 10^7$ | $3.81 \times 10^7$ | $2.25 \times 10^7$ | nm <sup>2</sup> |
| Nano-hardness ( $H$ )                | 712               | 788                | 1334               | MPa             |
| Elastic modulus ( $E$ )              | 72                | 76                 | 83                 | GPa             |
| Shear modulus ( $G = E/(2 + 2\nu)$ ) | 27                | 28.6               | 31.2               | GPa             |

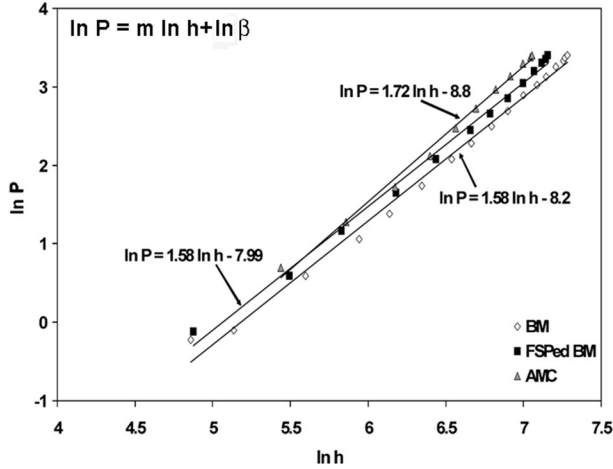


Fig. 5. Variation of applied load with the penetration depth in the nanoindentation tests.

composite. Another problem has been finding physical meaning for the dependence of the hardness/elastic modulus of the composite on those of its constituents. Here, modifying the present models to better identify the role of constituents on the mechanical properties of the fabricated composite was attempted.

The Hall–Petch equation is used to relate hardness ( $H$ ) to the mean-free path of moving dislocations as follows:

$$H = H_0 + \frac{K}{l} \quad (6)$$

where  $H_0$  stands for the intrinsic internal resistance against dislocation movement,  $K$  is the lock/unlock parameter of dislocations, and  $l$  is the dislocations mean-free path. For wrought polycrystals,  $l$  is directly related to  $d^{0.5}$ , where  $d$  is the average grain size. However, in the cast structures, the grain size has a marginal effect on strength, and  $l$  is equal to SDAS<sup>0.5</sup> (secondary dendrite arm spacing).<sup>38</sup> As shown in Fig. 1b and c, in the SZ of FSPed BM the dendritic structure has been disintegrated and transformed into an ultra-fine-grain matrix containing uniformly dispersed Si-rich particles. For this structure, Eq. 6 can be modified as follows:

$$H_{\text{FSPedBM}} = H_0 + Kd^{-1/2} + \Delta H_{\text{Si}} \quad (7)$$

where the term  $Kd^{-1/2}$  is the strengthening term of the grain boundaries and  $\Delta H_{\text{Si}}$  is the dispersion strengthening term due to the Si-rich particles. Referring to Table I, the sum of terms on the right-hand side of Eq. 7 for FSPed BM is equal to 788 MPa.

In the fabricated AMC, the total hardness ( $H_{\text{AMC}}$ ) can be related to the individual hardness values of the matrix ( $H_{\text{m-AMC}}$ ) and nano TiO<sub>2</sub> particles ( $H_p$ ) by using the law of mixture rule as follows:

$$H_{\text{AMC}} = f_m H_{\text{m-AMC}} + f_p H_p \quad (8)$$

where  $f$  stands for the phase fraction and indices  $m$  and  $p$  refer to the matrix and particles, respectively. Here,  $H_{\text{m-AMC}}$  is the sum of three terms: (1) the intrinsic internal resistance against dislocation movement ( $H_0$ ); (2) grain boundary strengthening ( $Kd^{-1/2}$ ); (3) dispersion hardening associated with the Si-rich particles and TiO<sub>2</sub> nanoparticles ( $\Delta H_{\text{Si}}$  and  $\Delta H_{\text{TiO}_2}$ ). Therefore,  $H_{\text{m-AMC}}$  can be written as follows:

$$H_{\text{m-AMC}} = H_0 + Kd^{-1/2} + \Delta H_{\text{Si}} + \Delta H_{\text{TiO}_2} \quad (9)$$

Combining Eqs. 7 and 9 yields:

$$H_{\text{m-AMC}} = H_{\text{FSPedBM}} + \Delta H_{\text{TiO}_2} \quad (10)$$

This means that the hardness of the matrix in the fabricated AMC is equal to the hardness of FSPed BM plus the contribution of TiO<sub>2</sub> nanoparticles. Based on the Orowan theory, an increase in the hardness of the matrix due to TiO<sub>2</sub> particles depends on the particle average spacing,  $\lambda$ , the shear modulus of the matrix,  $G$ , the magnitude of Burger's vector,  $b$ , and the average of the particle radius,  $r$ , and can be written as follows:<sup>39</sup>

$$\Delta H_{\text{TiO}_2} = \frac{0.13 Gb}{\lambda} \ln\left(\frac{r}{b}\right) \quad (11)$$

The average particle spacing,  $\lambda$ , is related to the volume fraction of particles ( $f_p$ ) and the average particle radius ( $r$ ) as follows:<sup>40</sup>

$$\lambda = 2r \left[ \left( \frac{1}{2f_p} \right)^{1/3} - 1 \right] \quad (12)$$

Assuming  $r = 50$  nm,  $f_p = 0.11$ ,  $G = 28.6$  GPa (Table I) and  $b = 0.4$  nm,<sup>41</sup> the average particle spacing is determined as 66 nm, which is in agreement with the result of Fig. 2b. By replacing the

values of  $G$ ,  $b$ ,  $r$  and  $\lambda$  in Eq. 11, the value of  $\Delta H_{\text{TiO}_2}$  is calculated as 109 MPa. Therefore, by using Eq. 10, the hardness of the matrix in the fabricated AMC ( $H_{\text{m-AMC}}$ ) is obtained as 897 MPa. Using the values of  $H_{\text{AMC}}$  and  $H_{\text{m-AMC}}$ , the hardness of  $\text{TiO}_2$  particles ( $H_p$ ) can be calculated and verified by the literature. Taking  $H_{\text{AMC}} = 1334$  MPa (according to Table I),  $H_{\text{m-AMC}} = 897$  MPa (as calculated by Eqs. 10, 11 and 12),  $f_p = 0.11$  and  $f_m = 0.89$ ,  $H_p$  is calculated as 4870 MPa. This value agrees well with the literature, which reports the hardness of the  $\text{TiO}_2$  nanostructure in the range of 4–10 GPa depending on the grain size and crystal structure.<sup>42,43</sup>

The Young's modulus of AMC can be related to the Young's modulus of constituents using different models. The shear lag method has been extensively used for the case of perfect interfacial bonding between the matrix and strengthening particles.<sup>44</sup> In this case, load easily transfers from the matrix to the particles through the interface. The shear lag method is often described as follows:<sup>44</sup>

$$E_c = f_p E_p [1 - \tanh(ns)/ns] + f_m E_m \quad (13)$$

$$n = (2E_m / [E_p(1 + \nu_m) \ln(1/f_p)])$$

where  $s$  is the aspect ratio of the strengthening phase and can be taken as 1 for spherical particles. Taking  $E_m = 76$  GPa (i.e.,  $E_{\text{FSPed-BM}}$  in Table I),  $E_p = E_{\text{TiO}_2} = 167$  GPa,<sup>42</sup>  $s = 1$  and  $\nu_m = 0.33$ , the value of  $E_c$  is calculated as 69.3 GPa. Referring to the experimental value of  $E_c = 83$  GPa in Table I, it is observed that the shear lag method underestimates the Young's modulus of AMC. It appears that the assumption of perfect interfacial bonding between the matrix and  $\text{TiO}_2$  particles is at the origin of the discrepancy between the calculated and experimental values of  $E_c$ . Therefore, the model should be modified based on the supposition of partial bonding between the matrix and  $\text{TiO}_2$  nanoparticles. The model can start with the law of mixture role for two extreme conditions of iso-stress (equal stress in the constituents) and iso-strain (equal strain in the constituents). These conditions are described by Eqs. 14a and 14b, respectively:<sup>43</sup>

$$E_{\text{in}} = f_p E_p + f_m E_m \quad (14a)$$

$$1/E_{\text{is}} = f_p/E_p + f_m/E_m \quad (14b)$$

where  $E_{\text{in}}$  and  $E_{\text{is}}$  refer to the Young's modulus of the composite in iso-strain and iso-stress conditions, respectively. Using the experimental values of  $f_p = 0.11$ ,  $f_m = 0.89$ ,  $E_m = 76$  GPa ( $E_{\text{FSPed-BM}}$  in Table I) and  $E_p = E_{\text{TiO}_2} = 167$  GPa,<sup>42</sup>  $E_{\text{is}}$  and  $E_{\text{in}}$  are predicted as 81 GPa and 86 GPa, respectively. It is evident that the iso-strain condition overestimates  $E_c$  ( $= 83$  GPa in Table I), while the iso-stress condition underestimates it. It is inferred that the actual condition lies between these two extremes. In the other words, stress and strain partitioning

occurs between the constituents of a composite under loading. The contribution coefficients of iso-stress and iso-strain conditions ( $a_{\text{is}}$  and  $a_{\text{in}}$ ) can be defined as follows:

$$a_{\text{is}} = \frac{E_{\text{in}} - E_c}{E_{\text{in}} - E_{\text{is}}} \quad (15)$$

$$a_{\text{in}} = \frac{E_c - E_{\text{is}}}{E_{\text{in}} - E_{\text{is}}} \quad (16)$$

It is observed that  $a_{\text{is}} + a_{\text{in}} = 1$ . Using the experimental values,  $a_{\text{is}}$  and  $a_{\text{in}}$  can be calculated as 0.6 and 0.4, respectively. Using the contribution coefficients of  $a_{\text{is}}$  and  $a_{\text{in}}$ , the Young's modulus of the composite can be written as follows:

$$E_c = a_{\text{in}} E_{\text{in}} + a_{\text{is}} E_{\text{is}} \quad (17)$$

By combining Eqs. 14a, 14b and 17, the Young's modulus of the composite can be written as a function of the Young's modulus of the A356 matrix ( $E_m$ ) and the Young's modulus of  $\text{TiO}_2$  particles ( $E_p$ ), as follows:

$$E_c = a_{\text{in}} f_p E_p + a_{\text{in}} f_m E_m + \frac{a_{\text{is}} E_m E_p}{f_p E_m + f_m E_p} \quad (18)$$

## Tribologic Behavior

The pin-on-disk test method was assigned to compare the wear behavior of fabricated samples with that of the BM. Figure 6 exhibits the weight loss, wear rate and friction coefficient as functions of wearing distance. The results show that for all samples the weight loss increases with an increase in the wear distance, while the wear rate declines. It is evident that at any given wear distance the amount of weight loss and the wear rate are higher for the BM than for the processed samples. The lowest weight loss and wear rate are obtained in the fabricated composite. The results in Fig. 6 indicate that there is a direct relationship between the hardness and tribologic properties. In the other words, it is implied that plastic deformation is the major microstructural mechanism underlying the wear of the studied samples. At the early stages of the wear test (short wear distances), the frictional heating simplifies the plastic flow of the surface against the tool. As the test proceeds to longer distances, the wear rate decreases for two reasons: first, the worn surface is gradually work hardened and therefore withstands further wear; second, the plasticized debris between the pin and surface decreases the contact surface.<sup>45</sup> On this basis, FSP promotes the wear resistance by increasing the work-hardening rate of material because of the microstructural modification as shown in Fig. 1. In AMC, the grain refinement and dispersion strengthening of  $\text{TiO}_2$  particles have a synergistic effect on

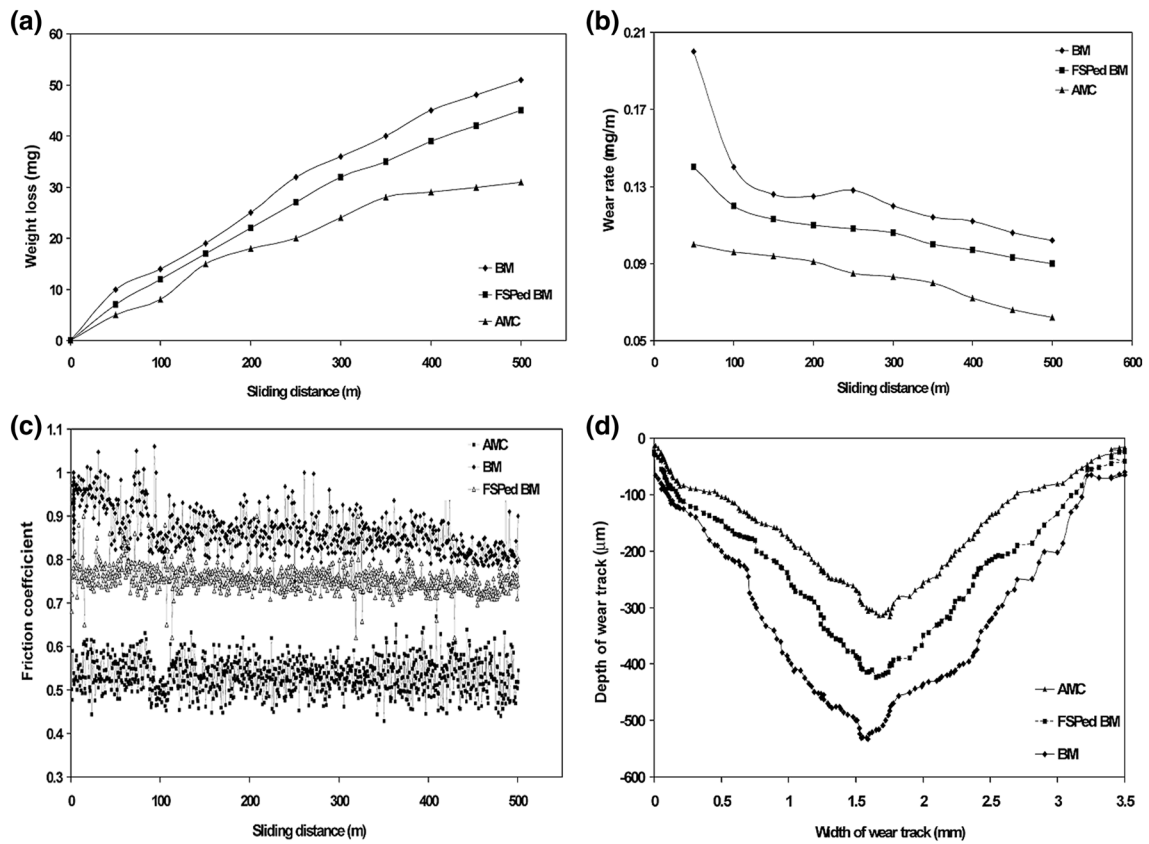


Fig. 6. Variations of the (a) weight loss, (b) wear rate, and (c) friction coefficient with the sliding distance and (d) the profile of depth of the wear track along the width of the wear track.

increasing the resistance against plastic deformation during wear. In similar studies on the wear behavior of surface composites, the decrease in weight loss has been attributed to load bearing by the reinforcing particles.<sup>46,47</sup> It has been approved that strengthening particles such as TiO<sub>2</sub> not only increase the wear resistance, but also change the wear mechanism from adhesive to abrasive.<sup>45,48</sup>

The change in the mechanism of wear in the fabricated AMC can be attributed to the higher hardness and decrease in the plastic deformation of the surface. In the AMC, wear debris adheres less to the surface, leading to reduced wear rate, as observed in Fig. 6b.

The friction coefficient values ( $\mu$ ) between the surface and wear tool are determined using the following equation:

$$\mu = \frac{F_f}{F_n} \quad (19)$$

here  $F_f$  and  $F_n$  are the friction and normal stress, respectively.

The values of  $\mu$  determined by analyzing the friction force and normal force (= 10 N) during the wear tests are reported in Fig. 6c. These results indicate that the friction coefficient decreases in the order of BM, FSPed BM and AMC. It appears that

the greater the hardness of the surface, the lower the friction coefficient will be.<sup>46</sup> Indeed, for a workpiece with lower hardness, more plastic debris adheres to the contact surfaces and results in a larger friction coefficient. Figure 6d clearly shows that the deepest wear fissures are obtained in the softest material, i.e., BM, and the depth of the fissure decreases with an increase in the hardness of the samples. In summary, these results confirm that an increase in the hardness of the workpiece leads to improved tribologic behavior. These findings agree well with previous investigations on the composites containing different reinforcing particles.<sup>46,49</sup>

The SEM micrographs of the worn surfaces are exhibited in Fig. 7. A few small micro-cracks and extensive surface delamination are the major marks of the worn BM surface in Fig. 7a. Delamination of surface layers is the general attribute of low-hardness materials and occurs in response to the coalescence of microcracks and voids in the layers underneath the worn surface.<sup>50,51</sup> On this basis, less adhesion and delamination on the worn surface of FSPed BM (Fig. 7b) can be ascribed to the hardness improvement by FSP. Unlike in Fig. 7a and b, the worn surface of the fabricated AMC in Fig. 7c is characterized by tiny grooves rather than adhesion and delamination.



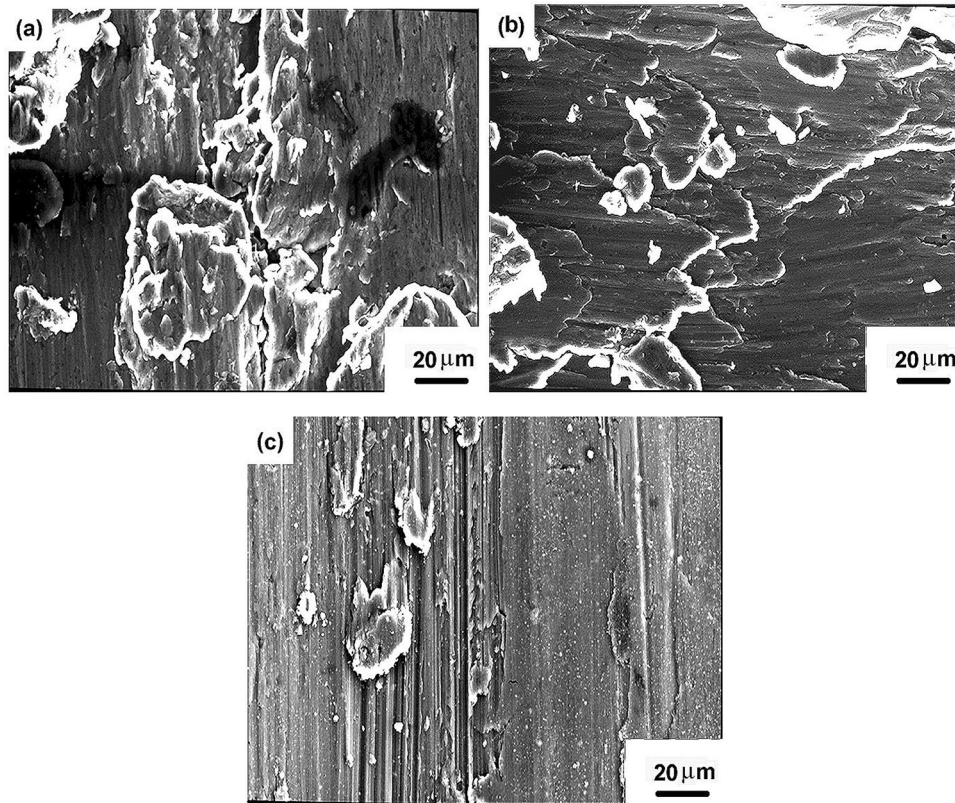


Fig. 7. Scanning electron micrographs of worn surfaces of (a) base metal, (b) FSPed base metal and (c) fabricated AMC under the wear load of 10 N.

It appears that the wear mechanism in AMC has changed from adhesive to abrasive wear, characterized by less delamination and more abraded marks. It is clear that this mechanism change is associated with the sharp increase in the hardness of AMC with respect to BM and FSPed BM, as indicated by Table I and Figs. 3 and 4. The grooves on the worn surface of Fig. 7c can be ascribed to trapping  $\text{TiO}_2$  particles between the wearing surfaces.<sup>48</sup>

## CONCLUSION

The individual effects of friction stir processing and nano  $\text{TiO}_2$  particles and their cooperative effect on the microstructure, mechanical and tribologic properties of cast A356 Al alloy were investigated in this research. The major results can be summarized as follows:

1. FSP resulted in the disintegration of the starting dendritic structure in the stirring zone (SZ). A uniform distribution of Si-rich particles within the matrix of alpha Al was obtained in the SZ. In the thermomechanically affected zone (TMAZ), the tree-type dendrites were transformed into nearly globular and uniform dendrites.
2. The microhardness test results showed that FSP leads to 13% improvement in the hardness of base metal. Further improvement in the hardness of the aluminum matrix composite (AMC) (about 52%; from 48 to 73 HV) was attributed to the superimposed effects of FSP and distribution of hard  $\text{TiO}_2$  nanoparticles in the Al matrix.
3. The results of the nanoindentation (NI) tests showed that FSP could improve the nano-hardness and elastic modulus of the BM by 10% and 6%, respectively. The nano-hardness and elastic modulus for AMC were improved by 69% and 9% with respect to the FSPed BM.
4. A combination of the law of mixture rule and Orowan's equation was used to establish a relationship between the nano-hardness of AMC with the hardness values of the constituents. Using the developed model, the roles of the FSPed matrix and  $\text{TiO}_2$  particles in the total nano-hardness of AMC were quantified.
5. It was found that the shear lag method underestimates the Young's modulus of the AMC. Assuming stress and strain partitioning between the constituents in AMC, the law of mixture rule was developed to correlate the Young's modulus of AMC with those of its constituents.
6. The results of wear tests showed that the wear resistance increases in the order of BM, FSPed BM and AMC. It was observed that there is an inverse relationship between the hardness and wear rate in the samples.
7. The SEM observations on the worn surfaces showed that the mechanism of wear in the BM

and FSPed BM is adhesive. However, abrasive wear is the prevailing wear mechanism in the fabricated composite.

### ELECTRONIC SUPPLEMENTARY MATERIAL

The online version of this article (<https://doi.org/10.1007/s11837-018-3092-9>) contains supplementary material, which is available to authorized users.

### REFERENCES

1. Y.C. Lin, Y.C. Xia, X.M. Chen, and M.S. Chen, *Comput. Mater. Sci.* 50, 227 (2010).
2. Y.C. Lin, Y.C. Xia, M.S. Chen, Y.Q. Jiang, and L.T. Li, *Comput. Mater. Sci.* 67, 243 (2013).
3. T.G. Durai, K. Das, and S. Das, *Mater. Sci. Eng.* A445–446, 100 (2007).
4. H. Mindivan, E.S. Kayali, and H. Cimenoglu, *Wear* 265, 645 (2008).
5. J. Guo, B.Y. Lee, Z. Du, G. Bi, M.J. Tan, and J. Wei, *JOM* 68, 2268 (2016).
6. M. Santella, A. Frederick, C. Degen, and T.-Y. Pan, *J. Miner. Met. Mater. Soc.* 58, 56 (2006).
7. Y. Zhao, X. Huang, Q. Li, J. Huang, and K. Yan, *Int. J. Adv. Manuf. Technol.* 78, 1437 (2015).
8. N. Nadammal, S.V. Kailas, J. Szpunar, and S. Suwas, *J. Miner. Met. Mater. Soc.* 67, 1014 (2015).
9. J. Qu, H. Xu, Z. Feng, D. Alan Frederick, L. An, and H. Heinrich, *Wear* 271, 1940 (2011).
10. M. Raaft, T.S. Mahmoud, Z.H.M. Akaria, and T.A. Khalifa, *Mater. Sci. Eng. A* 528, 5741 (2011).
11. E.R.I. Mahmoud, M. Takahashi, T. Shibayanagi, and K. Ikeuchi, *Wear* 268, 1111 (2010).
12. P. Asadi, M.K. Besharati Givi, A. Rastgoo, M. Akbari, V. Zakeri, and S. Rasouli, *Int. J. Adv. Manuf. Technol.* 63, 1095 (2012).
13. A. Dolatkhah, P. Golbabaee, M.K. Besharati Givi, and F. Molaiekiya, *Mater. Des.* 37, 458 (2012).
14. J. Guo, B.Y. Lee, Z. Du, G. Bi, M.J. Tan, and J. Wei, *J. Miner. Met. Mater. Soc.* 68, 2268 (2016).
15. A. Shafiei-Zarghani, S.F. Kashani-Bozorg, and A. Zarei-Hanzaki, *Mater. Sci. Eng. A* 500, 84 (2009).
16. M.A. Moghaddas and S.F. Kashani-Bozorg, *Mater. Sci. Eng. A* 559, 187 (2013).
17. N. Yuvaraj, S. Aravindan, and Vipin, *J. Mater. Res. Technol.* 4, 398 (2015).
18. S.F. Kashani-Bozorg and K. Jazayeri, *AIP Conf. Proc.* 1136, 715 (2009).
19. C. Maxwell Rejil, I. Dinaharan, S.J. Vijay, and N. Murugan, *Mater. Sci. Eng.* A552, 336 (2012).
20. N. Sun and D. Apelian, *JOM* 63 (11), 44 (2011).
21. S. Ahmadi, Sh. Kazemi, and A. Heidarpour, *J. Mater. Des. Appl.* 232, 287 (2018).
22. M. Akbari, A. Khalkhali, S.M.E. Keshavarz, and E. Sarikhani, *J. Mater. Des. Appl.* 232, 213 (2015).
23. M.H. Shojaeefard, M. Akbari, A. Khalkhali, and P. Asadi, *J. Mater. Des. Appl.* (2016). <https://doi.org/10.1177/1464420716642471>.
24. M. Akbari, A. Khalkhali, and S.M.E. Keshavarz, *J. Mater. Des. Appl.* (2016). <https://doi.org/10.1177/1464420716630569>.
25. S.A. Alidokht, A. Abdollah-zadeh, S. Soleymani, T. Saeid, and H. Assadi, *Mater. Charact.* 63, 90 (2012).
26. R. Yang, Z. Zhang, Y. Zhao, G. Chena, Y. Guo, M. Liu, and J. Zhang, *Mater. Charact.* 106, 62 (2015).
27. M.H. Shojaeefard, M. Akbari, P. Asadi, and A. Khalkhali, *Int. J. Adv. Manuf. Technol.* 91, 1391 (2017).
28. Z.Y. Ma, S.R. Sharma, and R.S. Mishra, *Metall. Mat. Trans.* 37A, 3323 (2006).
29. S. Meenia, F. Khan, S. Babu, R.J. Immanuel, S.K. Panigrahi, and G.D. Janaki Ram, *Mater. Charact.* 113, 134 (2016).
30. L. John Baruch, R. Raju, V. Balasubramanian, A.G. Rao, and I. Dinaharan, *Acta Metall. Sin.* 29, 431 (2016).
31. W.C. Oliver and G.M. Pharr, *J. Mater. Res.* 7, 1564 (1992).
32. K. Amouri, Sh. Kazemi, A. Momeni, and M. Kazazi, *Mater. Sci. Eng. A* 674, 569 (2016).
33. N. Sun and D. Apelian, *J. Miner. Met. Mater. Soc.* 63, 44 (2011).
34. Y. Li, F. Qin, C. Liu, and Z. Wu, *Metals* 524, 1 (2017).
35. H.R. Aniruddha Ram, P.G. Koppad, and K.T. Kashyap, *Mater. Sci. Eng. A* 559, 920 (2013).
36. J. Gilbert Kaufman, *Introduction to Aluminum Alloys and Tempers* (Materials Park, Ohio: ASM international, ASM, 2000).
37. A.C. Fischer-Cripps, *Nanoindentation*, 3rd ed. (Berlin: Springer, 2011).
38. E. Ghassemali, M. Riestra, T. Bogdanoff, B.S. Kumar, and S. Seifeddine, *Procedia Eng.* 207, 19 (2017).
39. A.S. Argon, *Strengthening Mechanisms in Crystal Plasticity* (Oxford: Oxford University Press, 2008).
40. F.A. Mirza and D.L. Chen, *Materials* 8, 5138 (2015).
41. N.A. Belov, A.A. Aksenov, and D.G. Eskin, *Iron in Aluminium Alloys: Impurity and Alloying Element* (Boca Raton: CRC Press, 2002).
42. D. Kaczmarek, J. Domaradzki, D. Wojcieszak, E. Prociow, M. Mazur, F. Placido, and St. Lapp, *J. Nano Res.* 18–19, 195 (2012).
43. D. Kaczmarek, D. Wojcieszak, J. Domaradzki, E. Prociow, F. Placido, S. Lapp, and R. Dylewicz, *Cent. Eur. J. Phys.* 9, 349 (2011).
44. T.W. Clyne, *Mater. Sci. Eng. A* 122, 183 (1989).
45. G. Huang, Y. Shen, R. Guo, and W. Guan, *Mater. Sci. Eng. A* 674, 504 (2016).
46. M. Akbari, M.H. Shojaeefard, P. Asadi, and A. Khalkhali, *Mater. Eng. Perform.* 26, 4297 (2017).
47. F. Ficici, *JOM* 66, 711 (2014).
48. A. Thangarasu, N. Murugan, and I. Dinaharan, *Procedia Eng.* 97, 590 (2014).
49. MdA Mehedi, K.M.H. Bhadhon, and M.N. Haque, *JOM* 68, 300 (2016).
50. A. Zmitrowicz, *J. Theor. Appl. Mech.* 44, 219 (2006).
51. U. Soy, A. Demir, and F. Findik, *Ind. Lubr. Technol.* 63/5, 387 (2011).